Journal of Power Sources 668 (2026) 239206

Contents lists available at ScienceDirect

Journal of Power Sources

journal homepage: www.elsevier.com/locate/jpowsour

Modeling the variability of thermal runaway behavior in large-format cylindrical cells with NMC-811 and LFP cathodes: A simulation study

Jan Schöberl [a,*], Stefan Schaeffler [b], Linus Grahl [a,c], Christoph Bach [a], Sebastian Ohneseit [d], Dominic Förstermann [c], Xuning Feng [e], Carlos Ziebert [d], Andreas Jossen [b], Markus Lienkamp [a]

[a] Technical University of Munich (TUM), School of Engineering & Design, Department of Mobility Systems Engineering, Institute of Automotive Technology, Boltzmannstr. 15, Garching, D-85748, Germany
[b] Technical University of Munich (TUM), School of Engineering & Design, Department of Energy and Process Engineering, Chair of Electrical Energy Storage Technology, Arcisstr. 45, Munich, D-80333, Germany
[c] Akkuracy Battery Testing GmbH, Herzog-Wilhelm-Strasse 25, Munich, D-80331, Germany
[d] Karlsruhe Institute of Technology (KIT), Institute for Applied Materials-Applied Materials Physics (IAM-AWP), Kaiserstrasse 12, Karlsruhe, D-76131, Germany
[e] State Key Laboratory of Intelligent Green Vehicle and Mobility, Tsinghua University, Beijing, 100084, China

HIGHLIGHTS

- Thermal runaway simulation framework for cylindrical NMC-811 and LFP cells.
- Modeling the variability of thermal runaway behavior in lithium-ion batteries.
- Model-based safety-related design of battery systems with cylindrical battery cells.

GRAPHICAL ABSTRACT

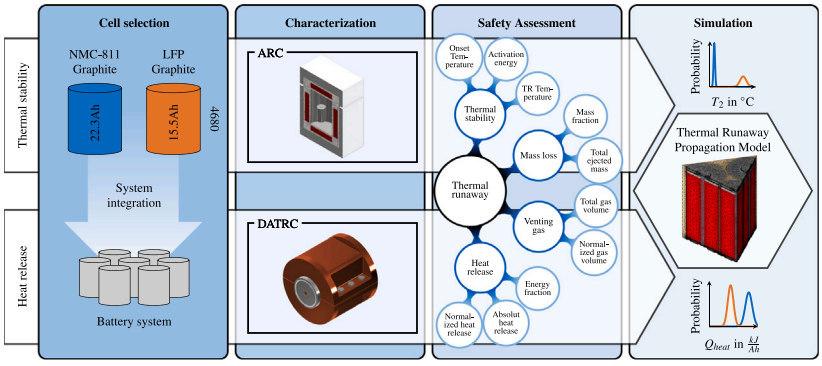

ARTICLE INFO

Dataset link: https://doi.org/10.5281/zenodo.14956641, https://doi.org/10.5281/zenodo.7707929, https://doi.org/10.5281/zenodo.14956635

Keywords:
Battery safety
Lithium-ion
Thermal runaway
Thermal runaway propagation
Thermal runaway modeling

ABSTRACT

Accurate thermal runaway modeling is required to mitigate thermal runaway propagation in battery systems. Since the thermal runaway of battery cells is a chaotic process, it is subject to high statistical variance. However, the variability of thermal runaway behavior is often not reflected in current simulation models. This paper presents a methodology for modeling the variability of thermal stability and heat release during thermal runaway of NMC-811 and LFP battery cells using accelerating rate calorimetry (ARC) and discretized autoclave thermal runaway calorimetry (DATRC) experiments. The thermal runaway model validation demonstrates a good agreement between simulation and experimental data within one standard deviation. In a simulation study, the thermal runaway simulation model was extended to a thermal runaway propagation model for a battery system with cylindrical 4680 cells. The simulation study revealed that thermal runaway propagation by heat transfer is unlikely in the case of a LFP cell chemistry. In contrast, thermal runaway propagation in similar systems with NMC-811 cells strongly depends on mass loss, cell spacing, and housing material. The simulation model improves an accelerated safety design concerning thermal runaway propagation in battery systems and enables a potential error estimation. Future research should focus on transferring the approach to other cell formats and validation on the system level.

* Corresponding author.
E-mail address: jan.schoeberl@tum.de (J. Schöberl).

https://doi.org/10.1016/j.jpowsour.2025.239206
Received 19 September 2025; Received in revised form 20 December 2025; Accepted 24 December 2025
Available online 22 January 2026

1. Introduction

Electric vehicles are established in the mobility market and continue expanding their market share [1]. However, several incidents involving electric vehicles catching fire have repeatedly brought battery safety into focus and raised safety concerns among customers [2]. A high level of battery safety is, therefore, one of the most important elements for the future success of electromobility. To eliminate these safety concerns in the future, legislators and even original equipment manufacturers (OEMs) are demanding increasingly higher safety requirements for battery systems, especially concerning mitigating thermal runaway propagation (TRP) [3–5]. The increased requirements make the safety-related design of battery packs for electric vehicles more challenging, as the experimental validation of the safety concept can be very time-consuming and expensive. For this reason, simulation-supported approaches for virtual design and validation of safety concepts are required to save time, costs, and resources in the early phase of battery development.

These approaches for an accelerated design of safety concepts require reliable thermal runaway (TR) simulation models, whereby the effects of cell selection on battery safety can be considered at an early stage of the battery development process. The basis for these models is a parameterization through a comprehensive characterization and safety assessment, which has already been described in a previous article by the authors [6]. In this work, the authors follow up on this work and present a TR simulation framework in which the parameters of the safety assessment can be transferred to a standardized simulation model.

Many publications in the literature already deal with the modeling of TR processes [7–22]. Richard and Dahn [7] modeled the thermal stability of lithiated graphite in electrolyte using Arrhenius equations. Hatchard et al. [8] presented a one-dimensional TR simulation model for a full cell. In further publications, the TR models were extended by further dimensions to a 3D model [15,23]. For example, Chen et al. [10] formulated a lumped 0D, axisymmetric 2D, and full 3D TR model and discussed their advantages and disadvantages. There are different approaches for modeling the reaction kinetics, which vary with regard to the degree of detail. Ren et al. [9] determined and parameterized the reaction kinetics for each cell component using differential scanning calorimetry (DSC) measurements and validated the TR model using accelerating rate calorimetry (ARC) measurements. Other publications formulate one or a few equations for the reaction kinetics based on ARC measurements, providing equally good results. Hoelle et al. [14] performed a parameter study to determine important parameters influencing the TR simulation. Thereby, mainly the mass loss during TR was identified as an important influencing parameter. Furthermore, three different modeling approaches for modeling the heat release during the TR were investigated, recommending a time-dependent and uniform modeling approach of the heat release. A further study by Schaeffler and Jossen [19] validated the recommended modeling approach by modeling and experimentally verifying the internal TRP in a single cell.

Most publications focus on modeling ternary batteries or other oxides as active material for the positive electrode [8–22]. Since TRP is equally relevant for other cell chemistries [24,25], TR models also exist for LFP batteries [26–32]. However, only a few TR models have a uniform methodology, meaning a direct simulation-based comparison between NMC and LFP is impossible. In addition, TRP is subject to high statistical variance [33,34] (e.g., due to the variability in heat release [34] and thermal stability [6]), which is almost always neglected in TRP modeling. The additional trend towards large-format cylindrical battery cells, such as the Tesla 4680 cell [35,36] or other cell formats from BMW's New Class [37], leads to a broad range of possible cell variants and poses new challenges for an accelerated safety-related system integration. Due to the different advantages and disadvantages of cell chemistries and formats [38,39], there is a wide range of variants in the market shares of battery cells, meaning that a suitable safety concept must also be found for each battery cell chemistry during system integration. However, existing TR models usually only apply to one cell chemistry of one specific cell and do not allow an adaptation for other cell chemistries. Furthermore, the TR is a chaotic process with high statistical variance that suffers from limited reproducibility [21,33,34,40]. Therefore, this work aims to provide a uniform TR simulation framework considering the variance of the heat release and thermal stability during TR to define potential error bands and confidence intervals for a more reliable safety assessment. The methodology is demonstrated based on the safety-related design of a battery system with cylindrical 4680 battery cells with NMC-811 and LFP cell chemistries, contributing to easier cell selection, optimized safety concepts, and simulation-based validation in the early phase of battery development.

1.1. Contributions

This work provides a uniform TR simulation model for cylindrical lithium-ion batteries with NMC-811 and LFP cathodes in the cell format 4680. The simulation framework aims to capture cell variants and statistical variances within a single simulation model, thereby simplifying safety-related design and enabling virtual simulation-based validation of safety concepts. To achieve these research goals, the main contributions of this study can be summarized as follows:

- **Thermal runaway simulation framework for cylindrical lithium-ion batteries with different cell chemistries**
  Development of a uniform TR simulation model and parameterization methodology for cylindrical NMC-811 and LFP battery cells to enhance transferability and adaptability to other battery cells in system development.
- **Modeling the variability of thermal runaway behavior for different cell chemistries**
  Integrating empirical uncertainties in heat release and thermal stability of NMC-811 and LFP batteries in the thermal runaway model to identify possible error bands and enable a worst-case assessment.
- **Methodology for model-based system integration in the safety-related design of battery systems with cylindrical battery cells**
  Upscaling the TR model to a TRP model and demonstrating a model-based system integration of the investigated battery cells in a simulation study to enable an accelerated and cost-effective safety assessment on the system level.

1.2. Structure of the article

The graphical abstract illustrates the structure of the article. Section 2 briefly describes the investigated cells in Section 2.1 and the experimental setup for characterizing thermal stability and heat release in Sections 2.2 and 2.3. An extensive safety assessment based on the safety parameters of the characterization can be found in [6]. This work focuses on model development, data extraction, and parameterization based on the safety characteristics for thermal stability and heat release in Section 3. Section 4 includes the validation of the simulation results with experimental data regarding thermal stability and heat release, as well as a simulation study on the safety-related integration of cylindrical 4680 cells with NMC-811 and LFP cathodes into a battery system. Finally, Section 5 summarizes the main findings of the work.

2. Experimental

This section describes the experimental setup for the characterization and validation of the TR simulation model's thermal stability and heat release. Sections 2.1 to 2.3 only provide a brief overview of the investigated battery cells and calorimetry test benches used in this work, as a more detailed description of the individual cells and methods has already been presented in [6].

2.1. Investigated cells

The battery cells selected for the TR model validation are commercially available lithium-ion batteries with the cell chemistries NMC-811 | graphite and LFP | graphite. Both cell chemistries are currently or in the future relevant for applications in automotive battery systems [38,39]. Although both battery cells have the same 4680 format, other minor differences are expected apart from the cell chemistry. For example, are minor differences in the cell geometry unavoidable as the cells come from different cell manufacturers. To increase comparability between the simulation results based solely on the change in cell chemistry, it is assumed that the cells have exactly the same cell geometry. For this purpose, the cell geometry, well-known from teardown studies [35] and computer tomography (CT) images [41], is merged into a uniform cell design. Even though the impact of this assumption on the simulation results is considered to be small, as the geometric differences are almost negligible. It should be noted that the fusion of the cell design is only performed for comparability purposes and can still cause minor implications. Therefore, a model geometry identical to the investigated cell is recommended to achieve the best simulation results

For a detailed description of the specifications and differences between the individual cells, the authors refer to [6].

2.2. Accelerating rate calorimetry

A common way to characterize the thermal stability of battery cells is accelerating rate calorimetry [42]. This method has established itself as very effective and precise as a high sensitivity and creation of quasi-adiabatic boundary conditions in the calorimeter allows an accurate analysis of the generated heat due to exothermic decomposition reactions during the thermal runaway over a wide temperature range. Further information on the execution of the experiments in the ARC used in this work can be found in [6]. The characteristic temperatures and the dynamics of the heat generation of several cells form the basis for the parameterization of the TR model and are described in more detail in Section 3.3. In order to validate the thermal stability exclusively on the heat generation of exothermic decomposition reactions and over the entire temperature range, it is also a common way to use the experimental data from the ARC test to validate the thermal stability, whereby the dynamics of the heat generation of the developed TR model should show a good agreement with the experimental data in Section 4.1. A further limited validation of the thermal stability is additionally provided in the simulation of the discretized autoclave thermal runaway calorimetry experiments, as described below.

2.3. Discretized autoclave thermal runaway calorimetry

Discretized autoclave thermal runaway calorimetry (DATRC) accurately measures the heat released during TR based on the temperature rise and known thermal masses of all calorimeter components in an isolated environment. The measurement data from DATRC experiments is therefore suitable for validating the heat release during TR in the simulation model.

The calorimeter setup used in this work is described in more detail in [6] and consists of two major assemblies that enable the decoupling between heat remaining in the cell body (solid fraction) and heat released via the venting gas (gas fraction). The solid fraction is especially relevant concerning TRP, as this heat fraction can cause TR of the neighboring cells via heat conduction. Please note that preventing TRP in battery systems also requires the isolation of the vent gas from the surrounding cells via vent paths to reduce convective heat transfer, which is recommended in many previous publications [25,43]. Therefore, a safety-related design based solely on conductive heat transfer is only feasible if the venting gas is completely insulated. As this is very uncommon in current battery systems and the convective heat input depends strongly on the geometry of the battery system, the convective heat transfer is varied via the heat transfer coefficient in the simulation study to represent different states of isolation and highlight the importance of vent gas isolation. In contrast, the conductive heat input is modeled in detail, as it can be precisely parameterized and validated using the solid fraction in the DATRC experiments.

The battery cells are thermally triggered with a constant temperature rate of $5\,^{\circ}\mathrm{C\,min^{-1}}$ applied to the cell surface in the DATRC experiment. In the actual test, this is realized with two heating foils attached to the cell surface of the investigated cells resulting in a maximum heating power of 300 W. Previous publications [21,34] have shown that the heat release and thermal stability are subject to deviations, which makes it challenging to validate the model with only a few experiments. For this reason, error bands are generated with the simulation model based on the normally distributed heat release and thermal stability. In this manner, the comparison between the experimental temperature data of the DATRC experiments and the simulated confidence intervals can be used for validation and plausibility of the heat release and the thermal stability.

3. Thermal runaway model

The thermal model used in this work was created in the commercial software *COMSOL Multiphysics 6.3*, which is based on the finite element method (FEM). The model focuses on the heat transfer within solids, whereby the governing equation for the energy balance of the solid in Cartesian coordinates can be formulated as follows:

$$\rho c_p \frac{dT}{dt} = \frac{\partial}{\partial x}\left(k_x \frac{\partial T}{\partial x}\right) + \frac{\partial}{\partial y}\left(k_y \frac{\partial T}{\partial y}\right) + \frac{\partial}{\partial z}\left(k_z \frac{\partial T}{\partial z}\right) + \sum \frac{\dot{Q}}{V} \tag{1}$$

where ρ represents the density, c_p the specific heat capacity, T the temperature, t the time, k_x, k_y and k_z the thermal conductivities in x,y, and z directions and $\sum \frac{\dot{Q}}{V}$ the sum of all heat sources within the respective solid.

3.1. Model geometry, mesh and boundary conditions

The model has been formulated as a three-dimensional (3D) model to represent internal temperature gradients in the cell. As the validation of the ARC tests requires long simulation times, an additional model was developed based on the 3D model by reducing the model to a 2D axisymmetric model. Since the boundary conditions in the ARC are also axisymmetric, the simplification is not expected to result in reduced model accuracy while significantly improving the simulation time. The model geometry for the ARC experiments is illustrated in Fig. 1(a). In the cell model, the minor differences in the cell design are compensated by merging the cell geometries of the two investigated cells in one uniform cell model to ensure results based solely on the change in cell chemistry. The tab design was created similarly to Tesla's tabless design, enabling heat conduction paths to the cell cap and bottom. As only the superposition of all decomposition reactions can be considered in the TR characterization methods used in this study, the jelly roll is not subdivided into individual electrode layers and is represented as one solid body (red area in Fig. 1).

For modeling the DATRC experiments, the assembly for absorbing the heat remaining in the cell body was transferred to a computer aided design (CAD) model and imported into the simulation program. In addition to the battery cell, the copper cell holder for monitoring the heat release and the heating foil for triggering the TR are represented in this model. In contrast, the insulation surrounding the copper cell holder is replaced by a convective heat flow boundary condition parameterized according to the fit to the experimental results. As the structure of the 3D model is also symmetrical, the simulation is performed with a reduced model, which is trimmed at the symmetry planes and corresponds to a quarter of the actual structure, as shown in Fig. 1(b).

For the simulation study on the system level, the thermal runaway model is extended to a TRP model. For this purpose, the trigger cell is

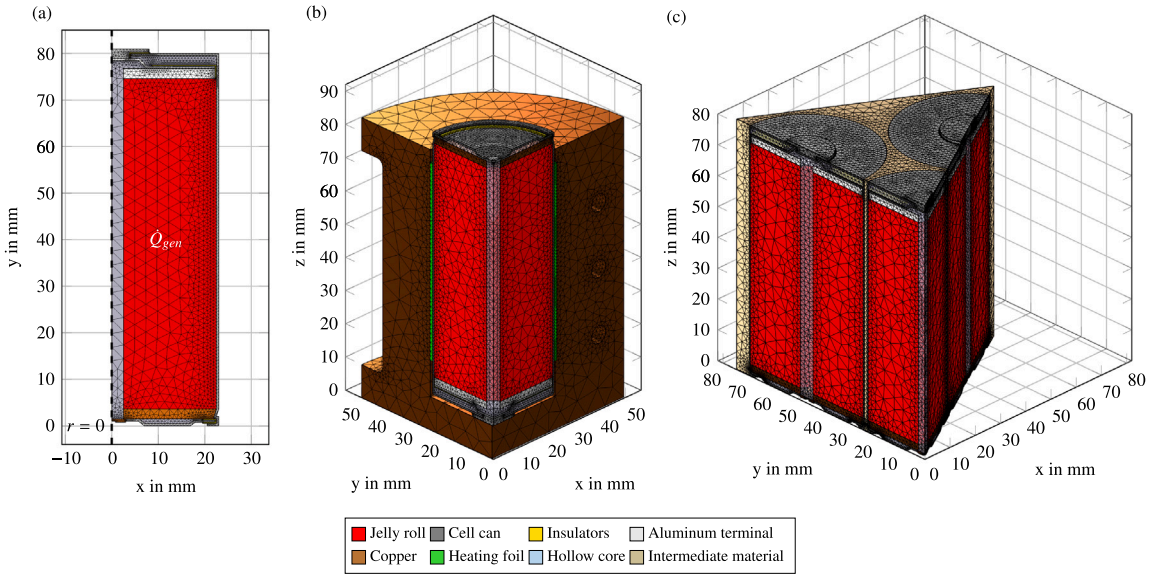

Fig. 1. Thermal runaway model geometry and mesh: (a) 2D axisymmetric thermal model of the battery cell in the ARC experiments. (b) 3D thermal model of the battery cell in a copper cell holder in the DATRC experiments. (c) 3D thermal model of the battery system in the TRP simulation study. Please note that only a quarter of the original geometry of the DATRC experiment and a sixth of the original geometry of the battery system in the TRP simulation study are modeled due to the symmetrical geometry. (For interpretation of the references to color in this figure, the reader is referred to the web version of this article.)

surrounded by six battery cells arranged in a honeycomb structure, representing the smallest possible system unit to replicate the temperature distribution within a battery system. Internal preliminary investigations have shown that the representation of further surrounding rows of battery cells does not significantly influence the simulation result, but substantially increases the simulation time. Therefore, further rows of battery cells are omitted in the model. It is assumed that the cells stand upright in the battery pack, with the safety vent facing the floor, and the electric contacting on the top of the cell cap. To ensure the mechanical integrity of the cells, the battery cells are embedded in a potting compound that covers the entire side wall. The material of the potting compound can be selected variably. This configuration can also often be found in battery systems from the manufacturer Tesla. Since the simulation model also has symmetries, only one-sixth is simulated to reduce the model size and thus the computational time. The distance between the battery cells can be freely adjusted in the model to investigate several system configurations for thermal runaway mitigation. The simulation study examines cell spacings of 1 and 2 mm. Fig. 1(c) shows the TRP model for a cell spacing of 1 mm.

3.2. Model parameterization

The data for parameterization of the thermal model is shown in Table 1. The areas associated with the material properties can be seen in Fig. 1. The parameterization of the dynamics and the heat release of the TR, as well as changes in material properties and other phenomena related to the TR, are considered and discussed separately in the subsequent sections.

The material properties of the jelly roll are modeled via the battery layers as a spirally wound solid, whereby the parameterization differs depending on the cell chemistry [44]. All hollow cores in the battery cell are assigned the thermal properties of nitrogen. The investigated intermediate material is a polyurethane interstitial potting compound with very low thermal conductivity ($\lambda_{PU} = 0.10\,\mathrm{W\,m^{-1}\,K^{-1}}$) commonly used in battery systems for automotive applications [45]. Please note that, unless otherwise stated, the respective material properties were taken from the *COMSOL* material library.

Table 1
Material properties of the model components. Values related to the jelly roll of NMC-811 and LFP cells correspond to [44].

Component	Density ρ [kg m^{-3}]		Spec. heat capacity c_p [Jkg^{-1}K^{-1}]		Therm. conductivity λ [Wm^{-1}K^{-1}]	
	NMC-811	LFP	NMC-811	LFP	NMC-811	LFP
Jelly roll ∥	2301.9[a]	2073.6[a]	1114	1307.7	22.448[b]	19.192[b]
Jelly roll ⊥	2301.9[a]	2073.6[a]	1114	1307.7	0.739[b]	0.828[b]
Cell can	7850		475		44.5	
Insulators	930		1700		0.2	
Aluminium	2700		900		238	
Copper	8960		385		400	
Hollow core	1.204		1005		0.025	
Heating foil	1150		1700		0.26	
Inter. material	400		1800		0.10	

[a] See also Eq. (12) for adaption during mass loss.
[b] See also Eq. (14) for post TR adaption.

3.3. Modeling heat release and thermal stability

The time and temperature dependent heat release $\dot{Q}_{heat}$ during the TR of a lithium-ion battery can be described by Eq. (2) with the total heat release ΔH_{tot} and the normalized reaction rate κ_x.

$$\dot{Q}_{heat}(t,T) = \Delta H_{tot} \cdot \eta_{energy} \cdot \kappa_x(t,T) \tag{2}$$

Since not all of the heat remains in the cell body, the total heat release is reduced by the mass loss of the jelly roll Δm_{JR} under the assumption that the energy fraction η_{energy} approximately equals the mass fraction of the jelly roll in Eq. (3) [6].

$$\eta_{energy} = \frac{\Delta H_{cell\,body}}{\Delta H_{tot}} \approx (1 - \Delta m_{JR}) \tag{3}$$

Please note that the heat release is temperature dependent and spatially resolved in the jelly roll highlighted by the red area in Fig. 1 and, therefore, the heat release is individual for each mesh volume element. The normalized reaction rate κ_x is commonly described by an Arrhenius equation. However, the approaches in the literature differ significantly in the number of source terms to describe the Arrhenius

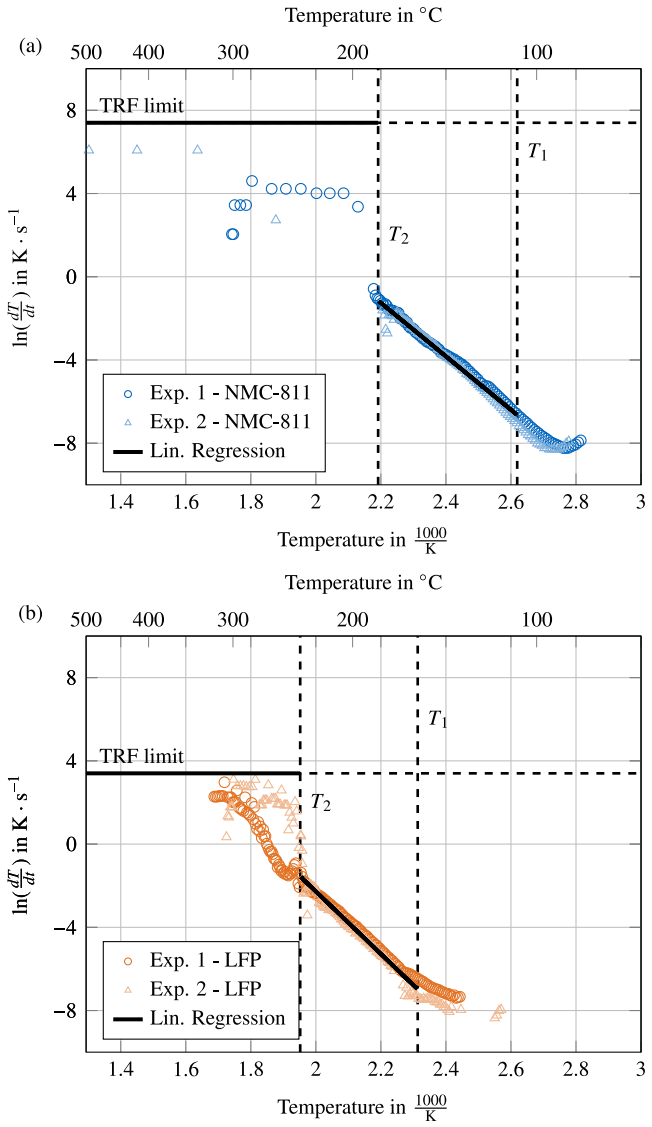

Fig. 2. Parameterization of the arrhenius equation by linear regression of the ARC measurement data between T_1 and T_2 and according to the TRF velocity for temperatures above T_2: (a) NMC-811 and (b) LFP.

equation. On the one hand, approaches with several source terms aim to describe the dynamics of individual decomposition reactions. On the other hand, approaches with only one source term describe the entirety of all decomposition reactions during TR. The latter has the advantage that the parameterization and computation effort are significantly lower, while providing an accuracy comparable to the first approach. For this reason, the thermal stability during TR is modeled based on an Arrhenius equation with one source term to describe the temperature dependence of the reaction rate κ in Eq. (4).

$$\kappa_x(t,T) = A(T) \cdot exp\left(-\frac{E_a(T)}{R \cdot T}\right) \cdot c_x(t,T) \tag{4}$$

where R is the universal gas constant, $A(T)$ is the temperature-dependent frequency factor and $E_a(T)$ is the temperature-dependent activation energy. The dimensionless concentration of reactants c is resolved and calculated according to Eq. (5).

$$c_x(t,T) = 1 - \int_0^t \kappa_x(t,T)\ dt \tag{5}$$

The activation energy and the frequency factor, also known as the pre-exponential factor, are defined as temperature-dependent values,

Table 2
Model parameters for parameterization of the TR model.

Parameter	Symbol	Unit	NMC-811	LFP
Cell capacity	C_{cell}	Ah	22.3	15.5
Ambient Temperature	T_∞	°C	20	20
Onset Temperature	T_1	°C	108.7	159.2
TR Temperature	T_2	°C	183.2	239.2
Std. Deviation T_2	σ_{T_2}	°C	1.67	6.94
Max. Temperature	T_3	°C	1325.1[a]	575.7[a]
TRF velocity ∥	$v_{TR,\parallel}$	mm s^{-1}	15	1.5
TRF velocity ⊥	$v_{TR,\perp}$	mm s^{-1}	3	0.3
Total heat release	ΔH_{tot}	kJ	487.7	182.9
Intersection y axis ($T < T_2$)	a_1	–	27.0	27.73
Intersection y axis ($T > T_2$)	a_2	–	7.4	3.4
Slope lin. regression ($T < T_2$)	b_1	–	−12.84	−15.01
Slope lin. regression ($T > T_2$)	b_2	–	0	0
Norm. heat release	$Q_{TR,norm}$	kJ Ah^{-1}	21.87	11.83
Std. Deviation $Q_{TR,norm}$	$\sigma_{Q_{TR,norm}}$	kJ Ah^{-1}	1.9	1.3
Elec. stored energy	ΔH_{ele}	kJ	297.0	178.6
Proportion nail trigger	α_{nail}	–	0.002	0.02

[a] Estimated via the heat release and thermal mass of the investigated cells.

as the reaction dynamics cannot be accurately mapped with a static parameterization. The thermal runaway can be characterized by three characteristic temperatures $\{T_1, T_2, T_3\}$ from ARC experiments [46], which were previously evaluated and analyzed in [6] for the investigated cells. According to the thermal runaway front (TRF) model by Feng et al. [47], these temperatures define two areas with different reaction dynamics. The first area is named transition zone, bordered by the temperatures T_1, which signals the onset of significant self-heating, and T_2, which is also known as the temperature of critical self-heating. Within these temperatures, a moderate but significant self-amplifying heat development is present. Based on the experimental data from the ARC tests, the reaction dynamics in this zone can be parameterized using the natural logarithm of the Arrhenius equation in Eq. (6) and a linear regression in Fig. 2.

$$\underbrace{ln\left(\frac{dT}{dt}\right)}_{y} \approx \underbrace{ln\left(A \cdot (T_2 - T_1)\right)}_{a_n} \underbrace{-\frac{E_a}{R}}_{b_n} \cdot \underbrace{\frac{1}{T}}_{x} \tag{6}$$

The results of the linear regression from Fig. 2 are shown in Table 2 for NMC-811 and LFP. The frequency factor $A(T)$ can then be calculated with Eq. (7) and the intersection with the y axis a_n.

$$A(T) = \begin{cases} \frac{exp(a_1)}{\Delta T}, & T < T_2 \\ \frac{exp(a_2)}{\Delta T}, & T > T_2 \end{cases} \tag{7}$$

The temperature increase ΔT resulting from the heat release in the jelly roll is calculated based on the jelly rolls density ρ_{jr}, heat capacity $c_{p,jr}$ and volume $V_{jr} = 111.53\,\text{cm}^3$ in Eq. (8).

$$\Delta T = \frac{\Delta H_{tot} \cdot \eta_{energy}}{\rho_{jr} \cdot c_{p,jr} \cdot V_{jr}} \tag{8}$$

Similarly, the activation energy $E_a(T)$ can be calculated via Eq. (9) and the slope of the linear regression b_n.

$$E_a(T) = \begin{cases} -b_1 \cdot R, & T < T_2 \\ 0, & T > T_2 \end{cases} \tag{9}$$

However, this method can only be used during moderate heat development at temperatures below T_2. Beyond the temperature T_2, the temperature development is significantly more dynamic and challenging for the calorimeter to track. During this phase, the temperature rate increases sharply, and a constant reaction rate is established, which is decisive for the TRF velocity. For this reason, this zone, which is defined by the temperatures T_2 and T_3, is also referred to as

the TRF zone. Due to the dynamics of the TR, the accelerating rate calorimeter can no longer keep the system adiabatic. In addition, the thermocouple attached to the cell surface may lose thermal contact due to the intensity of the reaction. As a result, the measurement data from the calorimeter no longer provides reliable information about the reaction behavior. For this reason, the parameterization of the TRF or the cell-internal TRP is based on a formula to calculate the TRF velocity and empirical data from [47]. The formula is converted to the normalized reaction rate in Eq. (10). The normalized reaction rate can be calculated using the TRF velocity v_{TR}, density ρ, heat capacity c_p, thermal conductivity λ, enthalpy of reaction ΔH, volume V and the factors α, β and γ. The partial calculations of the dimensionless factors can be found in the Appendix A.

$$\kappa = \frac{\left(v_{TR} \cdot \rho \cdot c_p\right)^2}{\lambda} \cdot \frac{V}{\Delta H} \cdot \frac{(\gamma - \beta)\left[\gamma + \beta\,(1-\alpha)\right]}{\beta\,(2-\alpha)^2} \tag{10}$$

The empirical data for the TRF velocity were selected to fit well with the experimentally measured data from [47] and show a uniform reaction rate regardless of the propagation direction. Thus, one parameter for a_2 can be calculated back using Eq. (7). In this temperature range, the frequency factor is characteristic for the overall reaction velocity, as the reaction rate no longer increases and therefore the activation energy equals zero, according to the TRF theory, as shown in Eq. (9). This is also graphically illustrated in Fig. 2 with the straight line with no gradient signalizing the TRF velocity limit. The transition of the two parameter sets at T_2 is implemented by a sigmoid function within a range of 40 K to improve the convergence of the solver. All parameters relevant for the calculation and the corresponding results are shown in Table 2.

3.4. Variability in heat release and thermal stability

The TR of lithium-ion batteries is a chaotic process subject to many stochastic variations. Therefore, the reproducibility of TR experiments is low, making it necessary to describe possible uncertainties in TR simulations.

For example, the analysis of several ARC experiments reveals that the temperature T_2 can vary and thus cause uncertainties in the thermal stability of the battery cell. In addition, multiple publications show that the heat release during thermal runaway is also subject to uncertainties and can be described by a normal distribution. Besides the parameters already mentioned, many other model parameters can also be subject to deviations. However, considering all theoretically possible uncertainties would mean an extremely high computational effort. For this reason, this study is limited to uncertainties of the thermal stability and heat release during TR described by normal distributions of the temperature T_2 and the normalized heat release $Q_{heat,norm}$ in Fig. 3.

Fig. 3(a) shows the normal distribution for the temperature T_2 for the cell chemistries NMC-811 and LFP. Please note that the mean value is cell-specific with 183.2 °C for NMC-811 and 239.2 °C for LFP and originates from two ARC experiments with the investigated 4680 cells from [6]. However, a larger sample of six ARC experiments with identical cell chemistries is used from [6] to determine the standard deviation, as previous investigations revealed that identical cell chemistries exhibit a comparable thermal stability. The results indicate a very reproducible behavior of the NMC-811 cells with 1.67 °C compared to the LFP cells with 6.94 °C. On the other hand, the heat release is very cell-specific. For this reason, six identical DATRC experiments were carried out for both investigated cells. The results can be seen in Fig. 3(b), where the mean value for the normalized heat release is 21.87 kJ Ah^{-1} for NMC-811 and 11.83 kJ Ah^{-1} for LFP. In contrast to the thermal stability, the heat release between the cell chemistries shows a comparable scatter with 1.9 kJ Ah^{-1} for NMC-811 and 1.3 kJ Ah^{-1} for LFP. The total heat release is normalized to the cell capacity C_{cell} to allow an easy model adaptation of the total heat release to other cells or energy densities for potential further studies using Eq. (11).

$$\Delta H_{tot} = Q_{TR,norm} \cdot C_{cell} \tag{11}$$

Fig. 3 highlights the areas for one and two standard deviations, representing a confidence level of 68 % and 95 % respectively, which is sufficient for model validation. All data used to determine the normal distributions can be found in Appendix B for temperature T_2 and Appendix C for normalized heat release $Q_{heat,norm}$.

3.5. Modeling mass loss

The material ejection during TR causes a change in the thermal properties, particularly of the jelly roll, which can significantly impact the simulation results [14]. Therefore, the mass loss during TR is simulated by adapting the jelly roll density in each volume element $\rho_{jr,x}$, whereby the jelly roll density after TR $\rho_{jr,postTR}$ matches the mass after TR. The jelly roll density is linked with the reaction concentration of the respective volume element c_x, and the initial jelly roll density $\rho_{jr,init}$ from Table 1 is adapted according to the progress of the reaction according to Eq. (12).

$$\rho_{jr,x}(c_x) = \rho_{jr,init} - (\rho_{jr,init} - \rho_{jr,postTR}) \cdot (1 - c_x) \tag{12}$$

In the *COMSOL* simulation model, this change in jelly roll density results in an energy loss in the system. To ensure system energy conservation, a correction term is introduced in Eq. (13), which maintains

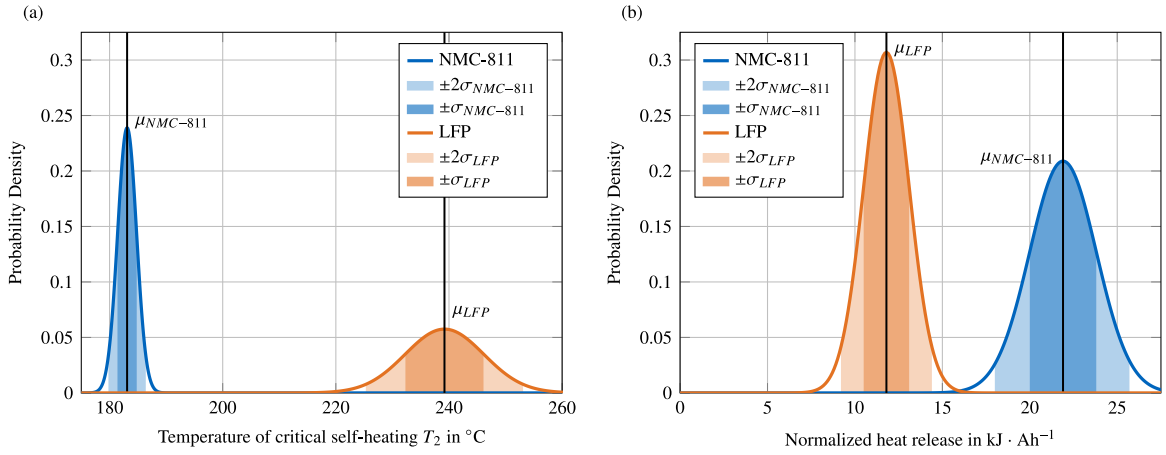

Fig. 3. Normal distributions of NMC-811 and LFP for (a) the critical self-heating temperature T_2 and (b) the normalized heat release $Q_{TR,norm}$. Please note that the normal distributions were each derived from six experiments in Appendices B and C, respectively.

the energy balance depending on the density change of the jelly roll.

$$\dot{Q}_{bal}(c_x, T) = \frac{d\rho_{jr}(c_x)}{dt} \cdot c_{p,jr} \cdot (T - T_{init}) \tag{13}$$

Furthermore, the thermal conductivity of the jelly roll changes after the TR due to the decomposition and degassing of the electrolyte. Similarly, structural damage to the jelly roll and gas layers between the electrodes can significantly impair thermal transfer. Unfortunately, to the best of the authors' knowledge, there are no reliable empirical values for thermal conductivity after TR of a battery cell. According to a fitting between experimental and simulation data by Pegel et al. [45], the thermal conductivity significantly decreases during TR. For this reason, the thermal conductivity of the jelly roll $\lambda_{jr,\parallel/\perp}$ is reduced by 50 % in this study with Eq. (14) after the reaction concentration reaches less than 10 %, as this represents a reasonable value according to [48].

$$\lambda_{jr,\parallel/\perp} = \begin{cases} \lambda_{jr,\parallel/\perp,init}, & c_x > 0.1 \\ \lambda_{jr,\parallel/\perp,init} \cdot 0.5, & c_x < 0.1 \end{cases} \tag{14}$$

3.6. Modeling venting

The venting of the cell under TR causes convective heat transfer to the surrounding cells. Since a complex calculation of the heat transfer by computational fluid dynamics (CFD) simulations exceeds the acceptable computational effort for a parameter variation, and these simulations are challenging to parameterize and validate, it was decided to consider cell venting as a convective boundary condition $\dot{Q}_{vent}$ in W/m^2 by Eq. (15).

$$\dot{Q}_{vent}(T) = h_{vent} \cdot (T - T_{vent}) \tag{15}$$

The heat transfer coefficient h_{vent} is varied in the simulation study, as this parameter is highly dependent on the isolation of the venting gas from the surrounding cells and also highly depends on many other geometric conditions in the battery pack, such as the height of the venting path or the battery cover. The venting gas temperature T_{vent} is taken from previous experimental studies and is set to 1000 °C for NMC-811 and 300 °C for LFP [25,49]. Since cell venting is caused by internal gas development during various decomposition reactions during thermal runaway, the boundary condition only applies if the average concentration of reactants in the trigger cell $\bar{c}_{x,trigger\ cell}$ is between 10 and 90 %, according to Eq. (16).

$$h_{vent} = \begin{cases} h_{vent}, & 0.9 > \bar{c}_{x,trigger\ cell} > 0.1 \\ 0, & 0.9 < \bar{c}_{x,trigger\ cell} < 0.1 \end{cases} \tag{16}$$

Outside these limits, it is assumed that a relevant gas development is no longer present to cause a significant heat transfer to other cells. In this way, the venting duration is defined by the reaction dynamics in Section 3.3. The modeled battery cells vent toward the bottom of the battery pack, separating the venting gas from the electrical path at the cell cap by the potting compound between the cells. This results in an area, highlighted in Fig. 4, where the venting boundary condition is present.

3.7. Modeling thermal runaway trigger

The cell is thermally triggered in the ARC and DATRC experiments for the simulation model validation. Therefore, the cell is triggered by an adiabatic boundary condition at a critical temperature level in the ARC simulation. On the other hand, a heating power is applied to the interface between the heating foil and the cell surface to realize a temperature ramp with a constant temperature rate of 5 °C min^{-1} in the DATRC simulation. However, the TR trigger is not defined by an experiment in the simulation study at the system level and can be randomly selected. For this reason, nail penetration is chosen as the TR trigger in this study, as it is a commonly used trigger that does not add additional energy to the system. For modeling the heat release during

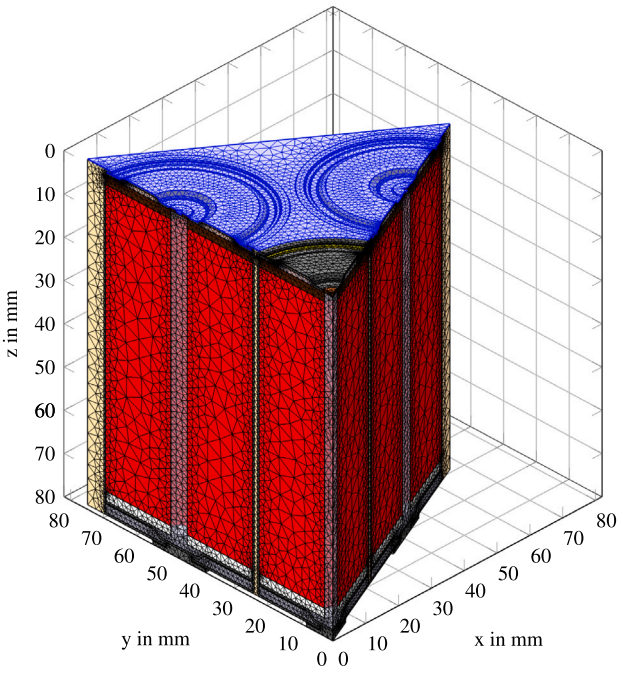

Fig. 4. Location of the venting boundary condition in the thermal model of the simulation study (blue area). Please note that the boundary condition applies at the bottom of the battery system illustrated in Fig. 1(c), and thus the geometry has been rotated accordingly. (For interpretation of the references to color in this figure, the reader is referred to the web version of this article.)

nail penetration $\dot{q}_{nail}$, an established method from Feng et al. [50] in Eq. (17) is used.

$$\dot{q}_{nail} = \frac{1}{V_{nail}} \cdot \alpha_{nail} \cdot \Delta H_{ele} \cdot f(\tau) \tag{17}$$

Here, V_{nail} is the volume of the nail in which the energy is released. The factor α_{nail} denotes the proportion of the total electric energy in the cell ΔH_{ele} released by an internal short circuit within a time period $f(\tau)$ defined by Feng et al. and can be found in [50]. To ensure a consistent heat balance in the model, the energy released by the internal short circuit is subtracted from the total energy released by the trigger cell.

4. Results and discussion

In the subsequent sections, the TR model is validated and applied. The validation of the thermal stability is performed on ARC experiments in Section 4.1. Followed by the validation of the heat release in Section 4.2 based on DATRC experiments that additionally supplement the validation of the thermal stability. The validation includes the variability of T_2 and $Q_{TR,norm}$, indicating potential error bands. This is followed by a simulation study regarding TRP in Section 4.3 based on the mean values of the previously determined normal distributions for thermal stability and heat release.

4.1. Validation thermal stability

Fig. 5 shows the simulated data from the TR model compared to the experimental data from two identical ARC tests for each investigated cell. The absolute temperature curve is shown in Figs. 5(a) and (b) and is normalized to the time of TR for better comparability. The simulated data show good agreement with the experimental data for both cell chemistries investigated. Even in the phases of rapid temperature development highlighted by a scope, no significant deviations can be detected.

A more detailed examination of the reaction dynamics can be made using the temperature rate plots in Fig. 5(c) and (d), which can better identify changes in the reaction dynamics due to the logarithmic representation. This illustration also better identifies the two phases of the reaction dynamics, which begin with a linear course and thus an exponential increase in the temperature rate in a logarithmic plot, and settle at a constant temperature rate for temperatures over T_2. This behavior can be observed in both cell chemistries and qualitatively well reproduced using the methodology described above. The reaction behavior for temperatures below T_2 can be very well reproduced for both cell chemistries.

Although the qualitative behavior matches the experimental data well for temperatures above T_2, quantitative deviations can be observed. For instance, the simulated temperature rate is an order of magnitude greater than the measured values in the NMC-811 cells. This deviation can be explained by the fact that a comparison with the experimental data is only possible to a limited extent in this range, as the temperature rate exceeds the maximum tracking rate of the calorimeter. In addition, the thermal coupling between the cell surface and the temperature sensor deteriorates increasingly due to TR, making it impossible to obtain a meaningful temperature measurement. Therefore, it can be assumed that the actual temperature rate is significantly higher than the experimentally measured values. Thus, the simulated temperature rate is not implausible, but challenging to validate.

In contrast, the simulated data of the LFP cells match the experimental data from experiment 2 even in the second phase of the TRF very well. A reason for this could be that the maximum temperature rate of LFP cells is several orders of magnitude lower compared to NMC-811 cells, allowing the calorimeter to track the temperature rate more accurately and preventing the loss of thermal contact between the cell and temperature sensor due to a comparatively moderate TR. However, experiment 1 shows a greater deviation from the simulated data, indicating that the reaction process is not reproducible, especially concerning LFP cells. The exact root cause of the different behavior cannot be determined, but the temperature data levels off again at temperatures above approximately 300 °C, resulting in an overall similar reaction behavior compared to experiment 2 with minor deviations. Complete coverage of all differences in the reaction behavior would mean extremely large uncertainties. For this reason, it was decided to represent the variability of thermal stability by the normal distribution of T_2 in Fig. 5. This provides reasonable error bands, illustrated for ±1 and ±2 standard deviations in Fig. 3(a). In Figs. 5(a) and (b), the differences are hardly noticeable due to the normalization to the TR, as they are mainly evident in the time shift and not in the shape of the temperature curve. Additional validation and demonstration of the variability in thermal stability are therefore provided in Section 4.2.

4.2. Validation heat release

The heat released during TR is validated by comparing the simulated and experimental temperature data from the DATRC experiments in Fig. 6. For the investigated NMC-811 cell, an energy fraction of

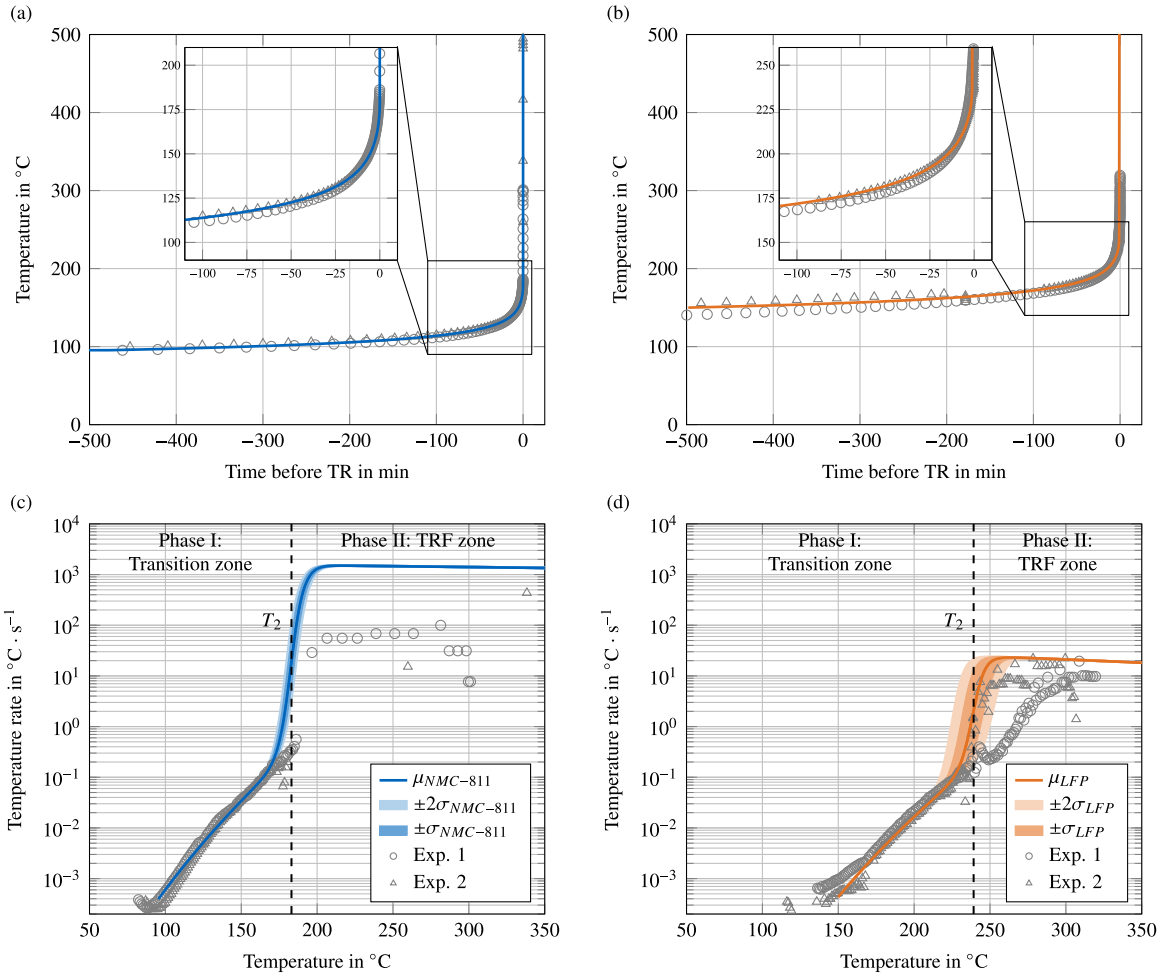

Fig. 5. Validation of the thermal stability of the TR model based on measurement data from ARC experiments. Comparison of measured and simulated surface temperature of the (a) NMC-811 and (b) LFP battery cell. Comparison of measured and simulated temperature rate of the (c) NMC-811 and (b) LFP battery cell with visualization of the individual phases in the TR reaction dynamics.

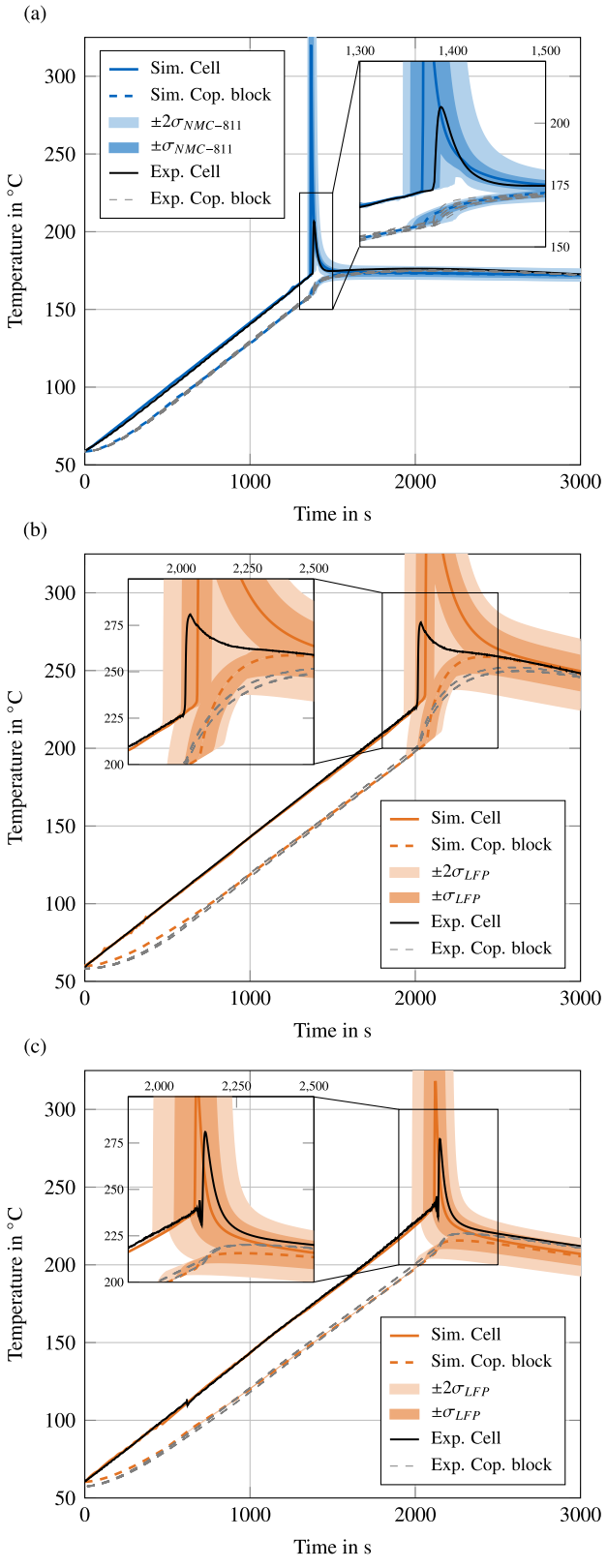

Fig. 6. Validation of the thermal stability and heat release of the TR model based on measurement data from DATRC experiments. Comparison of the measured and simulated cell surface and copper block temperature: DATRC experiment with (a) an NMC-811 cell with a energy fraction η_{energy} of 6 %, (b) an LFP cell with a energy fraction η_{energy} of 54 % and (c) an LFP cell with a energy fraction η_{energy} of 12 %.

6 % equaling a jelly roll mass loss of 94 % was observed and used in the simulation in Fig. 6(a). The results indicate good agreement with the experimental data. TR was observed in the experiment shortly after the mean value of the simulation, but the results are still within one standard deviation over the entire time. The peak temperature of the cell surface in the simulation is significantly higher than the measured value at the time of TR, which may be due to the thermal connection and inertia of the thermocouple. As expected from the high mass loss, not much energy remains in the copper cell holder, resulting in a slight temperature increase in the copper block. The simulation model accurately reproduces the temperature increase and subsequently reaches a temperature level that indicates that the heat release was well reproduced. Due to the low absolute temperature level, there is only a small room for deviations.

During the test series of the LFP battery cells, it was noticed that the mass loss can vary depending on the opening of the safety vent, which can influence the mass and energy fraction of the battery cell [6]. For this reason, two datasets with an energy fraction of 54 % representing a low jelly roll mass loss of 36 % in Fig. 6(b) and an energy fraction of 12 % equaling a high jelly roll mass loss of 88 % in Fig. 6(c) are used in the case of the LFP cell, where the different behavior was observed, in order to validate the simulated mass and energy balances. The TR in the cell with a low mass loss of 36 % occurs at a surface temperature of 225 °C, while it occurs slightly later at approximately 237 °C in the cell with a high mass loss of 88 %. These differences are likely not due to the different mass losses but rather to the variation in thermal stability, as both lie within one standard deviation of the simulated error ranges. The subsequent heat release is primarily within one standard deviation and is therefore well simulated. Only in the dynamics shortly after TR are minor deviations observed within the range of two standard deviations. This shows that the thermal properties after and during TR are challenging to model, and at the same time highlights the need for further research.

4.3. Simulation study

The simulation study at the system level demonstrates a potential application of the validated TR simulation model for optimizing the safety design of battery systems. For this purpose, the cell chemistry, cell spacing, and cell can material are varied in the system model from Fig. 1(c). For each system configuration, a TRP risk map is created, which indicates the maximum JR temperature of the adjacent cell and thus the potential risk of TRP [45]. In addition, the mass loss and the heat transfer coefficient of the venting are varied between 0.1 and 0.9 and between 0 and 750 $\mathrm{Wm^{-2}K^{-1}}$ in each TRP risk map. Here, the mass loss is decisive for the conductive heat path, and the heat transfer coefficient is decisive for the convective heat path to the neighboring cells. This enables a better interpretation and identification of safe system configurations and the derivation of design guidelines. Please note that all simulations are based on the average values of the temperature of critical self-heating T_2 and the normalized heat release $Q_{TR,norm}$.

4.3.1. Influence cell chemistry

Fig. 7 shows the TRP risk maps of the two investigated cells for a cell spacing of 1 mm and a steel cell can. The TRP risk map for the NMC-811 cell in Fig. 7(a) indicates that TRP highly depends on the remaining heat in the cell body. A mass loss of less than 50 % is not sufficient to prevent TRP. However, the simulation also shows that with a mass loss of 0.9, as in the real cell, no propagation will likely occur. Even with a lower mass loss of 0.7, it seems possible to prevent TRP, but probably not in all cases, considering that the simulations were performed based on the average heat release and T_2 values. A strong dependence of TRP on the heat transfer coefficient of the venting and thus on the convective heat path is not observed. The heat input through the convective heat path strongly depends on the heat conduction paths

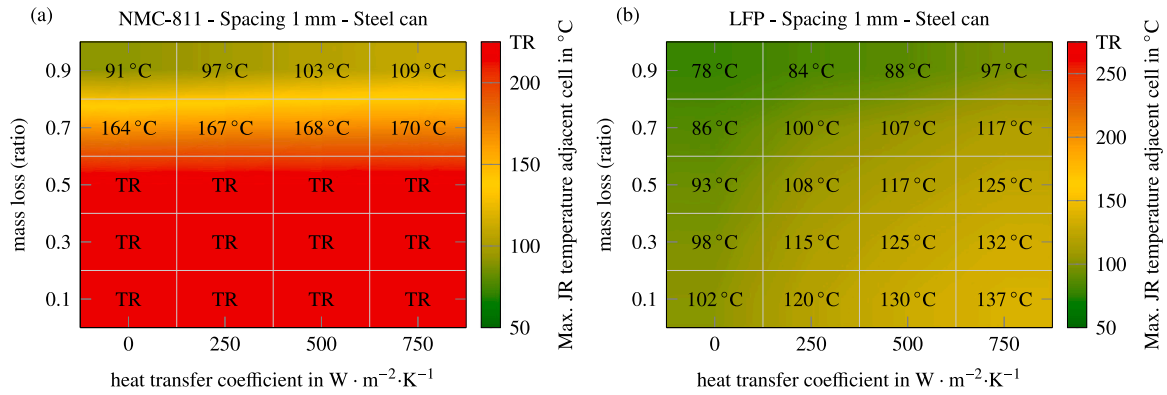

Fig. 7. TRP risk maps for (a) NMC-811 and (b) LFP cells with a steel cell can and a cell spacing of 1 mm. Please note that the color bars are scaled differently depending on the temperature of the critical self-heating T_2 of the respective cell chemistries. (For interpretation of the references to color in this figure, the reader is referred to the web version of this article.).

from the cell surface to the jelly roll. These paths lead, on the one hand, through the cell housing and, on the other hand, through the terminals for electrical contacting. For this reason, the cause of the reduced heat input by convection may be the low thermal conductivity of the steel housing or the implementation of the tab design, which is a hybrid of a tab and tabless design in this study. Please note that the results can, therefore, vary greatly depending on the modeling of the tab design. In contrast to the NMC-811 cell, the results for the investigated LFP cell in Fig. 7(b) indicate exclusively safe system configurations with a cell spacing of just 1 mm. Even with a mass loss of 0.1 and a strong venting boundary condition of 750 $Wm^{-2}K^{-1}$, the maximum JR temperature of the neighboring cell is uncritical, so it can be assumed with a very high degree of certainty that no TRP will occur in terms of the LFP cells. On the one hand, this can be explained by the lower absolute heat release and, on the other hand, by the higher temperature of critical self-heating T_2 compared to the NMC-811 cell, meaning that safety-critical conditions are more difficult to reach. The results conclude that TRP is theoretically impossible in battery systems with cylindrical 4680 LFP cells if a comparable intermediate material is used and a cell spacing of >1 mm is maintained. In the case of the LFP cells, it is possible to reduce the cell spacing to avoid overengineering. However, the potting compound's flow behavior in manufacturing processes may impose restrictions on the minimum cell spacing, limiting the spacing to 1 mm [45]. For these reasons, it is reasonable to say that such a configuration of the battery system is oversized from a safety point of view concerning TRP. A workaround for LFP cells would be considering large-format prismatic cells, reducing system complexity, and possibly providing higher energy density at the pack level. However, since cases with [25] and without [44] TRP were previously reported in the case of large-format prismatic LFP cells, a new safety assessment of the system configuration according to the provided methodology is essential. Since the configuration shown is already uncritical in the case of an LFP cell chemistry, only the NMC-811 cell will be considered in the following investigations.

4.3.2. *Influence cell spacing*

Fig. 8 shows the results for system configurations with 1 and 2 mm cell spacing. Increasing the cell spacing increases the thermal resistance between the TR cell and adjacent cells, shifting the entire TRP risk map along the mass loss axis. According to the simulation results, it is possible to prevent TRP with a cell spacing of 2 mm, even with low mass losses of up to 0.3. Increasing the cell spacing significantly affects the conductive heat path to neighboring cells. A similar effect can be achieved by reducing the thermal conductivity of the interlayer material. The simulation model does not represent the influence of the increased cell spacing on the convective heat path. However, it can be assumed that it only becomes relevant at larger cell spacings and can be neglected when considering cell spacings between 1 and 2 mm.

With an aluminum cell can, TRP can be prevented at all considered mass losses if heat input by venting can be excluded entirely. Accordingly, a cell spacing of 1 to 2 mm is sufficient to prevent TRP, as almost the entire heat output during thermal runaway can be released in the cell body without the occurrence of a propagation through the conductive heat path. Cell spacing greater than 2 mm would therefore be oversized in this case, and more attention should be paid to handling the venting gas to further improve the safety design.

Please also note that adjusting the cell spacing inevitably results in a change in the volumetric energy density of the battery pack. Increasing the cell spacing from 1 to 2 mm is therefore associated with a reduction in volumetric energy density of approximately 4 %.

4.3.3. *Influence cell can material*

A comparison of steel and aluminum cell can materials reveals that they produce different TRP risk maps. When comparing the maximum jelly roll temperature of the adjacent cell without or with slight venting of 250 $Wm^{-2}K^{-1}$, the temperatures are lower for the cell with an aluminum cell can. This can be related to the higher thermal conductivity of aluminum, which distributes heat more evenly throughout the cell or even pack and prevents local hotspots, as previously reported by Pegel et al. [45]. Therefore, battery cells with aluminum housings are more robust against conductive heat transfer paths, minimizing the appearance of hotspots. However, in cases with stronger venting and a heat transfer coefficient greater than 500 $Wm^{-2}K^{-1}$, the results are reversed, and the maximum jelly roll temperatures of the adjacent cell are often higher for the cell with an aluminum cell can. It is therefore evident that the high conductivity of the cell housing also dissipates more heat from the cell surface, causing the cell to absorb more heat overall via the convective heat path. The increased heat input caused by venting thus leads to a higher risk of TRP in the event of strong venting. The advantages of an aluminum cell can for improving the safety design are therefore present but limited, as the heat input caused by venting is higher and side wall ruptures cannot be excluded due to the low melting point of aluminum at 660 °C [51]. The choice of material for the cell can thus significantly influence the safety design and its further optimization, whereby the conductive heat path is particularly relevant in the case of a steel cell can. In contrast, an aluminum cell can better handle the heat input via conduction, but also leads to a stronger superposition by the convective heat path, making measures against venting more relevant.

5. Summary and conclusions

This paper presents a methodology for modeling the variability of the TR behavior in battery cells with different cell chemistries to enable an accelerated safety assessment and design in the early phase

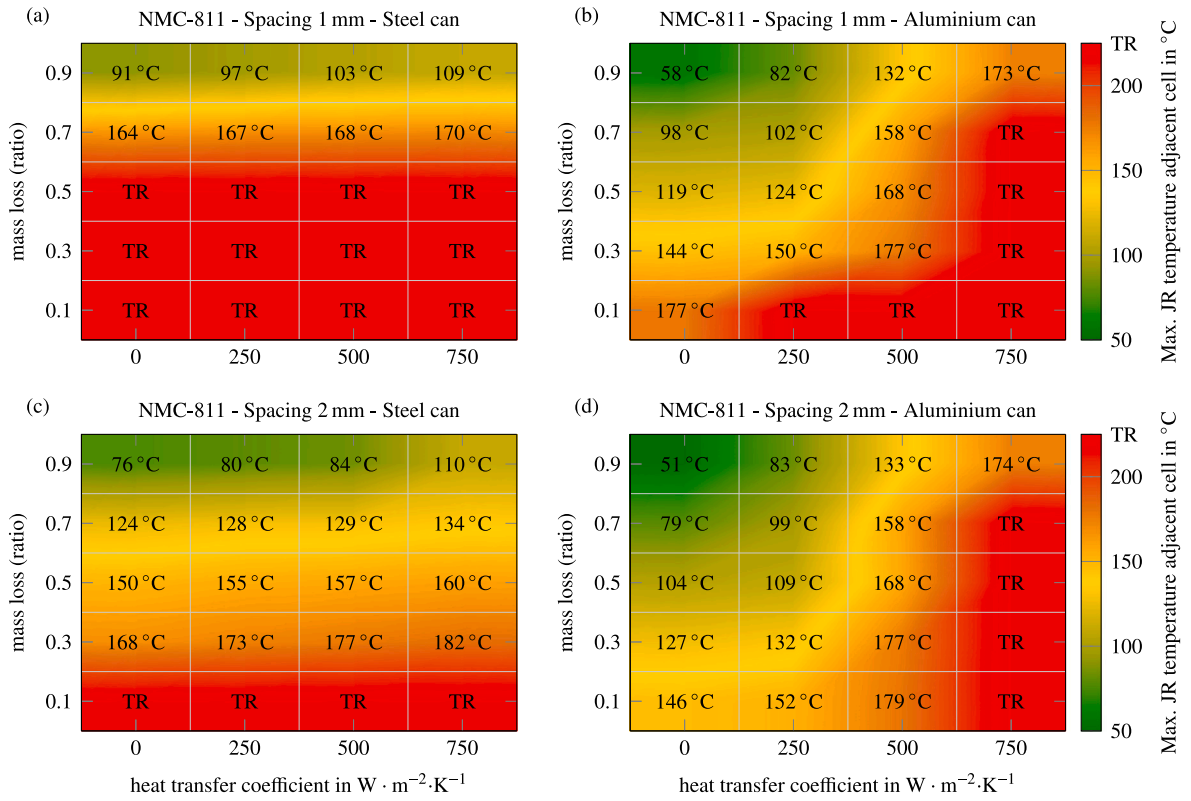

Fig. 8. TRP risk maps for NMC-811 cells with different cell spacings and cell can materials: (a) 1 mm spacing and steel can, (b) 1 mm spacing and aluminium can, (c) 2 mm spacing and steel can, and (d) 2 mm spacing and aluminium can.

of battery development. The investigations focus on the variability in the thermal stability and heat release of NMC-811 and LFP cells and a simulation study on the system level to identify safe system configurations. The investigations revealed the following results, and can be summarized as follows:

(1) **Thermal runaway simulation framework for different cell chemistries:** A uniform data extraction and parameterization methodology for different cell chemistries was presented. In addition, the reaction process was divided into two phases and implemented according to the TRF model, which allows the reaction dynamics of both cell chemistries to be well represented.
(2) **Modeling the variability of thermal runaway behavior:** The variability of thermal stability and heat release was determined experimentally and implemented in the simulation model to replicate the variance of TR behavior. The validation of the simulation model demonstrated that the experimental data are within one standard deviation and thus represent a realistic representation of the error bands.
(3) **Influence of cell chemistry:** A simulation study investigated the influence of cell chemistry on TRP. The results indicate that TRP can occur in the case of cylindrical NMC-811 cells in the 4680 format, but it highly depends on further system parameters (e.g., venting, mass loss, cell spacing, and cell can material). In contrast, no propagation occurs in the LFP counterpart, regardless of the system configuration.
(4) **Influence of cell spacing and cell can material:** The safety-related design can be enhanced by changes in cell spacing and cell can material. While increasing the cell spacing only reduces conductive heat transfer, changing the cell can affect the conductive and convective heat input. An aluminum cell housing is more robust against conductive heat input due to a fast heat distribution within the cell as a result of its high thermal conductivity. On the other hand, convective heat input also increases through venting, which means that the safety advantages of aluminum cell cans are limited in cases of strong venting.

The presented TR model for NMC-811 and LFP battery cells provides a valuable basis for an accelerated and reliable safety design of battery systems by considering the variation in thermal stability and heat release. For further considerations, future research should focus on the statistical analysis of the venting behavior and its modeling to enhance the results of this study. In addition, the modeling approach should also be validated on the system level to substantiate the quantitative results and define possible error bands of the failure propagation. This enables further improvement in the accelerated model-based safety design of battery systems.

Abbreviations

ARC	Accelerating rate calorimetry
CAD	Computer aided design
CFD	Computational fluid dynamics
CT	Computer tomography
DATRC	Discretized autoclave thermal runaway calorimetry
DSC	Differential scanning calorimetry
FEM	Finite element method
JR	Jelly roll
LFP	$LiFePO_4$
NMC	$Li(Ni_xCo_yMn_z)O_2$
OEM	Original equipment manufacturer
TR	Thermal runaway
TRF	Thermal runaway front
TRP	Thermal runaway propagation

CRediT authorship contribution statement

Jan Schöberl: Writing – review & editing, Writing – original draft, Visualization, Validation, Software, Project administration, Methodology, Investigation, Data curation, Conceptualization. **Stefan Schaeffler:** Writing – review & editing, Validation, Software, Methodology, Investigation. **Linus Grahl:** Writing – review & editing, Visualization, Investigation, Data curation. **Christoph Bach:** Writing – review & editing, Visualization, Software, Investigation. **Sebastian Ohneseit:** Writing – review & editing, Investigation, Data curation. **Dominic Förstermann:** Writing – review & editing, Investigation, Data curation. **Xuning Feng:** Writing – review & editing, Supervision. **Carlos Ziebert:** Writing – review & editing, Supervision, Resources, Funding acquisition. **Andreas Jossen:** Writing – review & editing, Supervision, Resources, Funding acquisition. **Markus Lienkamp:** Writing – review & editing, Supervision, Resources, Funding acquisition.

Declaration of competing interest

The authors declare that they have no known competing financial interests or personal relationships that could have appeared to influence the work reported in this paper.

Acknowledgments

This work was financially supported by the German Federal Ministry for Economic Affairs and Energy, Germany (BMWK) within the project "ContAeroFilter" under grant number ZF4648103CL9, by the German Federal Ministry of Education and Research (BMBF), Germany within the projects "BetterBat" under grant number 03XP0362C and "TUBE" under grant number 03XP0425 and by the Helmholtz Association, Germany, in the programme Materials and Technologies for the Energy Transition (MTET), and we want to express our gratitude for the funding. This work contributes to the research performed at CELEST (Center of Electrochemical Energy Storage Ulm-Karlsruhe). We thank TUM.Battery for promoting battery research by providing an interdisciplinary network of experts.

Appendix A. Determination of the dimensionless factors for normalized reaction rate calculation

The temperature factor β is calculated by T_2 and T_3 in Eq. (A.1).

$$\beta = \frac{T_3 - T_2}{2} \tag{A.1}$$

The shape factor α is determined in Eq. (A.2) with T_2, T_3 and the ambient temperature T_∞.

$$\alpha = \frac{T_2 - T_\infty}{T_3 - T_2} \tag{A.2}$$

The shape factor α also contributes to the calculation of shape factor γ in Eq. (A.3).

$$\gamma = \left[(T_3 - T_\infty) - \alpha(T_2 - T_\infty) - \frac{1}{2}(T_3 - T_2)(1 - \alpha^2)\right] \tag{A.3}$$

Appendix B. Determining the variability in the thermal stability

See Table B.

Table B
Calculation of the mean value and standard deviation of the temperature of critical self-heating T_2 for NMC-811 and LFP based on six ARC experiments for each cell chemistry with cells in the cell formats 18650, 21700, and 4680, according to the results in [6]. Please note that the mean value is only based on the values from the experiments with the 4680 cells.

Exp.	Chemistry	Cell format	T_2 [°C]	μ_{T_2} [°C]	σ_{T_2} [°C]
1	NMC-811	18 650	182.6		
2	NMC-811	18 650	181.9		
3	NMC-811	21 700	182.6	183.2[a]	1.67
4	NMC-811	21 700	182.4		
5	NMC-811	4680	181.9		
6	NMC-811	4680	181.2		
7	LFP	18 650	251.9		
8	LFP	18 650	249.6		
9	LFP	21 700	248.0	239.2[a]	6.94
10	LFP	21 700	257.1		
11	LFP	4680	242.2		
12	LFP	4680	236.2		

[a] Only based on the experiments with the 4680 cells.

Table C
Calculation of the mean value and standard deviation of the normalized heat release for NMC-811 and LFP based on six DATRC experiments for each cell chemistry with the investigated cells in the cell format 4680.

Exp.	Chemistry	Cell format	$Q_{TR,norm}$ [kJ Ah^{-1}]	$\mu_{Q_{TR,norm}}$ [kJ Ah^{-1}]	$\sigma_{Q_{TR,norm}}$ [kJ Ah^{-1}]
1	NMC-811	4680	19.6		
2	NMC-811	4680	21.7		
3	NMC-811	4680	20.1	21.87	1.9
4	NMC-811	4680	25.4		
5	NMC-811	4680	22.9		
6	NMC-811	4680	21.5		
7	LFP	4680	10.3		
8	LFP	4680	12.2		
9	LFP	4680	11.9	11.83	1.3
10	LFP	4680	13.3		
11	LFP	4680	10.0		
12	LFP	4680	13.3		

Appendix C. Determining the variability in the heat release

See Table C.

Data availability

We want to give any researcher access to our results without any limits. The measurement data of all ARC experiments are available via the following digital object identifiers (DOI): https://doi.org/10.5281/zenodo.14956641 (18650 cells), https://doi.org/10.5281/zenodo.7707929 (21700 cells), and https://doi.org/10.5281/zenodo.14956635 (4680 cells). For the data on the DATRC experiments, the authors refer to Appendix C.

References

[1] Zentrum für Sonnenenergie- und Wasserstoff-Forschung Baden-Württemberg, Data service renewable energies - global EV registrations, 2024, URL https://www.zsw-bw.de/en/media-center/data-service.html. (Accessed on 18 August 2025).

[2] N. Shanmugavel, C. Alagappan, J. Balakrishnan, Acceptance of electric vehicles: A dual-factor approach using social comparison theory and technology acceptance model, Res. Transp. Bus. Manag. 45 (2022) 100842, http://dx.doi.org/10.1016/j.rtbm.2022.100842.

[3] Y. Chen, Y. Kang, Y. Zhao, L. Wang, J. Liu, Y. Li, Z. Liang, X. He, X. Li, N. Tavajohi, B. Li, A review of lithium-ion battery safety concerns: The issues, strategies, and testing standards, J. Energy Chem. 59 (2021) 83–99, http://dx.doi.org/10.1016/j.jechem.2020.10.017.

[4] X. Lai, J. Yao, C. Jin, X. Feng, H. Wang, C. Xu, Y. Zheng, A review of lithium-ion battery failure hazards: Test standards, accident analysis, and safety suggestions, Batteries 8 (11) (2022) 248, http://dx.doi.org/10.3390/batteries8110248.

[5] V. Ruiz, A. Pfrang, A. Kriston, N. Omar, P. van den Bossche, L. Boon-Brett, A review of international abuse testing standards and regulations for lithium ion batteries in electric and hybrid electric vehicles, Renew. Sustain. Energy Rev. 81 (2018) 1427–1452, http://dx.doi.org/10.1016/j.rser.2017.05.195.

[6] J. Schöberl, S. Ohneseit, S. Schaeffler, D. Förstermann, L. Grahl, A. Jossen, C. Ziebert, M. Lienkamp, Thermal runaway characterization of cylindrical lithium-ion and sodium-ion batteries with various sizes and energy contents, J. Power Sources 648 (2025) 237240, http://dx.doi.org/10.1016/j.jpowsour.2025.237240.

[7] M.N. Richard, J.R. Dahn, Part I: Accelerating Rate Calorimetry Study on the Thermal Stability of Lithium Intercalated Graphite in Electrolyte I. Experimental.

[8] T.D. Hatchard, D.D. MacNeil, A. Basu, J.R. Dahn, Thermal model of cylindrical and prismatic lithium-ion cells, J. Electrochem. Soc. 148 (7) (2001) A755, http://dx.doi.org/10.1149/1.1377592.

[9] D. Ren, X. Liu, X. Feng, L. Lu, M. Ouyang, J. Li, X. He, Model-based thermal runaway prediction of lithium-ion batteries from kinetics analysis of cell components, Appl. Energy 228 (2018) 633–644, http://dx.doi.org/10.1016/j.apenergy.2018.06.126.

[10] H. Chen, J.E.H. Buston, J. Gill, D. Howard, R.C.E. Williams, E. Read, A. Abaza, B. Cooper, J.X. Wen, A simplified mathematical model for heating-induced thermal runaway of lithium-ion batteries, J. Electrochem. Soc. 168 (1) (2021) 010502, http://dx.doi.org/10.1149/1945-7111/abd64c.

[11] P.T. Coman, E.C. Darcy, C.T. Veje, R.E. White, Modelling li-ion cell thermal runaway triggered by an internal short circuit device using an efficiency factor and arrhenius formulations, J. Electrochem. Soc. 164 (4) (2017) A587–A593, http://dx.doi.org/10.1149/2.0341704jes.

[12] P.T. Coman, S. Rayman, R.E. White, A lumped model of venting during thermal runaway in a cylindrical lithium cobalt oxide lithium-ion cell, J. Power Sources 307 (2016) 56–62, http://dx.doi.org/10.1016/j.jpowsour.2015.12.088.

[13] G. Guo, B. Long, B. Cheng, S. Zhou, P. Xu, B. Cao, Three-dimensional thermal finite element modeling of lithium-ion battery in thermal abuse application, J. Power Sources 195 (8) (2010) 2393–2398, http://dx.doi.org/10.1016/j.jpowsour.2009.10.090.

[14] S. Hoelle, F. Dengler, S. Zimmermann, O. Hinrichsen, 3D thermal simulation of lithium-ion battery thermal runaway in autoclave calorimetry: Development and comparison of modeling approaches, J. Electrochem. Soc. 170 (1) (2023) 010509, http://dx.doi.org/10.1149/1945-7111/acac06.

[15] G.-H. Kim, A. Pesaran, R. Spotnitz, A three-dimensional thermal abuse model for lithium-ion cells, J. Power Sources 170 (2) (2007) 476–489, http://dx.doi.org/10.1016/j.jpowsour.2007.04.018.

[16] D. Kong, G. Wang, P. Ping, J. Wen, Numerical investigation of thermal runaway behavior of lithium-ion batteries with different battery materials and heating conditions, Appl. Therm. Eng. 189 (2021) 116661, http://dx.doi.org/10.1016/j.applthermaleng.2021.116661.

[17] J.K. Ostanek, W. Li, P.P. Mukherjee, K.R. Crompton, C. Hacker, Simulating onset and evolution of thermal runaway in li-ion cells using a coupled thermal and venting model, Appl. Energy 268 (2020) 114972, http://dx.doi.org/10.1016/j.apenergy.2020.114972.

[18] P. Peng, Y. Sun, F. Jiang, Thermal analyses of LiCoO2 lithium-ion battery during oven tests, Heat Mass Transf. 50 (10) (2014) 1405–1416, http://dx.doi.org/10.1007/s00231-014-1353-x.

[19] S. Schaeffler, A. Jossen, In situ measurement and modeling of internal thermal runaway propagation within lithium-ion cells under local overheating conditions, J. Power Sources 614 (2024) 234968, http://dx.doi.org/10.1016/j.jpowsour.2024.234968.

[20] Q. Wang, P. Ping, X. Zhao, G. Chu, J. Sun, C. Chen, Thermal runaway caused fire and explosion of lithium ion battery, J. Power Sources 208 (2012) 210–224, http://dx.doi.org/10.1016/j.jpowsour.2012.02.038.

[21] L. Zhang, S. Yang, L. Liu, P. Zhao, Cell-to-cell variability in li-ion battery thermal runaway: Experimental testing, statistical analysis, and kinetic modeling, J. Energy Storage 56 (2022) 106024, http://dx.doi.org/10.1016/j.est.2022.106024.

[22] Y. Zhang, W. Mei, P. Qin, Q. Duan, Q. Wang, Numerical modeling on thermal runaway triggered by local overheating for lithium iron phosphate battery, Appl. Therm. Eng. 192 (2021) 116928, http://dx.doi.org/10.1016/j.applthermaleng.2021.116928.

[23] R. Spotnitz, J. Franklin, Abuse behavior of high-power, lithium-ion cells, J. Power Sources 113 (1) (2003) 81–100, http://dx.doi.org/10.1016/S0378-7753(02)00488-3.

[24] Z. Huang, X. Li, Q. Wang, Q. Duan, Y. Li, L. Li, Q. Wang, Experimental investigation on thermal runaway propagation of large format lithium ion battery modules with two cathodes, Int. J. Heat Mass Transfer 172 (2021) 121077, http://dx.doi.org/10.1016/j.ijheatmasstransfer.2021.121077.

[25] J. Schöberl, M. Ank, M. Schreiber, N. Wassiliadis, M. Lienkamp, Thermal runaway propagation in automotive lithium-ion batteries with NMC-811 and LFP cathodes: Safety requirements and impact on system integration, ETransportation 19 (2024) 100305, http://dx.doi.org/10.1016/j.etran.2023.100305.

[26] S. Abada, M. Petit, A. Lecocq, G. Marlair, V. Sauvant-Moynot, F. Huet, Combined experimental and modeling approaches of the thermal runaway of fresh and aged lithium-ion batteries, J. Power Sources 399 (2018) 264–273, http://dx.doi.org/10.1016/j.jpowsour.2018.07.094.

[27] P.J. Bugryniec, J.N. Davidson, S.F. Brown, Computational modelling of thermal runaway propagation potential in lithium iron phosphate battery packs, Energy Rep. 6 (2020) 189–197, http://dx.doi.org/10.1016/j.egyr.2020.03.024.

[28] E. Kwak, J.-H. Kim, S.H. Hong, K.-Y. Oh, Detailed modeling investigation of thermal runaway pathways of a lithium iron phosphate battery, Int. J. Energy Res. 46 (2) (2022) 1146–1167, http://dx.doi.org/10.1002/er.7235.

[29] H. Sadeghi, F. Restuccia, Pyrolysis-based modelling of 18650-type lithium-ion battery fires in thermal runaway with LCO, LFP and NMC cathodes, J. Power Sources 603 (2024) 234480, http://dx.doi.org/10.1016/j.jpowsour.2024.234480.

[30] T. Sun, L. Wang, D. Ren, Z. Shi, J. Chen, Y. Zheng, X. Feng, X. Han, L. Lu, L. Wang, X. He, M. Ouyang, Thermal runaway characteristics and modeling of LiFePO4 power battery for electric vehicles, Automot. Innov. 6 (3) (2023) 414–424, http://dx.doi.org/10.1007/s42154-023-00226-3.

[31] Y. Zhang, S. Cheng, W. Mei, L. Jiang, Z. Jia, Z. Cheng, J. Sun, Q. Wang, Understanding of thermal runaway mechanism of LiFePO4 battery in-depth by three-level analysis, Appl. Energy 336 (2023) 120695, http://dx.doi.org/10.1016/j.apenergy.2023.120695.

[32] Y. Zhang, L. Song, J. Tian, W. Mei, L. Jiang, J. Sun, Q. Wang, Modeling the propagation of internal thermal runaway in lithium-ion battery, Appl. Energy 362 (2024) 123004, http://dx.doi.org/10.1016/j.apenergy.2024.123004.

[33] B. Mulder, J. Schöberl, K.P. Birke, Thermal propagation test bench with multi pouch cell setup for reproducibility investigations, Batteries 9 (9) (2023) 447, http://dx.doi.org/10.3390/batteries9090447.

[34] W.Q. Walker, J.J. Darst, D.P. Finegan, G.A. Bayles, K.L. Johnson, E.C. Darcy, S.L. Rickman, Decoupling of heat generated from ejected and non-ejected contents of 18650-format lithium-ion cells using statistical methods, J. Power Sources 415 (2019) 207–218, http://dx.doi.org/10.1016/j.jpowsour.2018.10.099.

[35] M. Ank, A. Sommer, K. Abo Gamra, J. Schöberl, M. Leeb, J. Schachtl, N. Streidel, S. Stock, M. Schreiber, P. Bilfinger, C. Allgäuer, P. Rosner, J. Hagemeister, M. Rößle, R. Daub, M. Lienkamp, Lithium-ion cells in automotive applications: Tesla 4680 cylindrical cell teardown and characterization, J. Electrochem. Soc. 170 (12) (2023) 120536, http://dx.doi.org/10.1149/1945-7111/ad14d0.

[36] J. Gorsch, J. Schneiders, M. Frieges, N. Kisseler, D. Klohs, H. Heimes, A. Kampker, M. Muñoz Castro, E. Siebecke, Contrasting a BYD blade prismatic cell and tesla 4680 cylindrical cell with a teardown analysis of design and performance, Cell Rep. Phys. Sci. 6 (3) (2025) 102453, http://dx.doi.org/10.1016/j.xcrp.2025.102453.

[37] BMW Group AG, Round battery cells for the neue klasse, 2022, URL https://www.bmwgroup.com/en/news/general/2022/gen6.html. (Accessed 05 January 2024.

[38] S. Link, C. Neef, T. Wicke, Trends in automotive battery cell design: A statistical analysis of empirical data, Batteries 9 (5) (2023) 261, http://dx.doi.org/10.3390/batteries9050261.

[39] S. Hasselwander, M. Meyer, I. Österle, Techno-economic analysis of different battery cell chemistries for the passenger vehicle market, Batteries 9 (7) (2023) 379, http://dx.doi.org/10.3390/batteries9070379.

[40] K. Masalkovaitė, P. Gasper, D.P. Finegan, Predicting the heat release variability of li-ion cells under thermal runaway with few or no calorimetry data, Nat. Commun. 15 (1) (2024) 8399, http://dx.doi.org/10.1038/s41467-024-52653-3.

[41] A. Condon, B. Buscarino, E. Moch, W.J. Sehnert, O. Miles, P.K. Herring, P.M. Attia, A dataset of over one thousand computed tomography scans of battery cells, Data Brief 55 (2024) 110614, http://dx.doi.org/10.1016/j.dib.2024.110614.

[42] S. Ohneseit, P. Finster, C. Floras, N. Lubenau, N. Uhlmann, H.J. Seifert, C. Ziebert, Thermal and mechanical safety assessment of type 21700 lithium-ion batteries with NMC, NCA and LFP cathodes–Investigation of cell abuse by means of accelerating rate calorimetry (ARC), Batteries 9 (5) (2023) 237, http://dx.doi.org/10.3390/batteries9050237.

[43] S. Hoelle, S. Scharner, S. Asanin, O. Hinrichsen, Analysis on thermal runaway behavior of prismatic lithium-ion batteries with autoclave calorimetry, J. Electrochem. Soc. 168 (12) (2021) 120515, http://dx.doi.org/10.1149/1945-7111/ac3c27.

[44] J. Yao, X. Lai, S. Wong, Y. Peng, X. Rui, M. Zhang, C. Jin, C. Xu, X. Feng, Y. Zheng, Investigating thermal runaway propagation characteristics and configuration optimization of the hybrid lithium-ion battery packs, Int. J. Heat Mass Transfer 233 (2024) 126021, http://dx.doi.org/10.1016/j.ijheatmasstransfer.2024.126021.

[45] H. Pegel, M. Autenrieth, S. Schaeffler, A. Jossen, D.U. Sauer, Design guidelines to prevent thermal propagation and maximize packing density within battery systems with tabless cylindrical lithium-ion cells, J. Energy Storage 86 (2024) 111275, http://dx.doi.org/10.1016/j.est.2024.111275.

[46] X. Feng, S. Zheng, X. He, L. Wang, Y. Wang, D. Ren, M. Ouyang, Time sequence map for interpreting the thermal runaway mechanism of lithium-ion batteries with LiNixCoyMnzO2 cathode, Front. Energy Res. 6 (2018) http://dx.doi.org/10.3389/fenrg.2018.00126.

[47] X. Feng, F. Zhang, J. Feng, C. Jin, H. Wang, C. Xu, M. Ouyang, Propagation dynamics of the thermal runaway front in large-scale lithium-ion batteries: Theoretical and experiment validation, Int. J. Heat Mass Transfer 225 (2024) 125393, http://dx.doi.org/10.1016/j.ijheatmasstransfer.2024.125393.

[48] X. Feng, S.K. WONG, T. Chen, M. Ouyang, An automatic identification method of thermal physical parameter for lithium-ion batteries suffering from thermal runaway, J. Energy Storage 83 (2024) 110358, http://dx.doi.org/10.1016/j.est.2023.110358.

[49] H. Pegel, S. Schaeffler, A. Jossen, D.U. Sauer, Extensive experimental thermal runaway and thermal propagation characterization of large-format tabless cylindrical lithium-ion cells with aluminum housing and laser welded endcaps, J. Electrochem. Soc. 170 (12) (2023) 120512, http://dx.doi.org/10.1149/1945-7111/ad0cd3.

[50] X. Feng, L. Lu, M. Ouyang, J. Li, X. He, A 3D thermal runaway propagation model for a large format lithium ion battery module, Energy 115 (2016) 194–208, http://dx.doi.org/10.1016/j.energy.2016.08.094.

[51] A.F. Holleman, Lehrbuch der Anorganischen Chemie, 100th ed., Walter de Gruyter GmbH, Berlin/Boston, 1985, URL https://ebookcentral.proquest.com/lib/kxp/detail.action?docID=5761637.